

Differentiable Weightless Controllers: Learning Logic Circuits for Continuous Control

Fabian Kresse¹ Christoph H. Lampert¹

Abstract

We investigate whether continuous-control policies can be represented and learned as discrete logic circuits instead of continuous neural networks. We introduce Differentiable Weightless Controllers (DWCs), a symbolic-differentiable architecture that maps real-valued observations to actions using thermometer-encoded inputs, sparsely connected boolean lookup-table layers, and lightweight action heads. DWCs can be trained end-to-end by gradient-based techniques, yet compile directly into FPGA-compatible circuits with few- or even single-clock-cycle latency and nanojoule-level energy cost per action. Across five MuJoCo benchmarks, including high-dimensional Humanoid, DWCs achieve returns competitive with weight-based policies (full precision or quantized neural networks), matching performance on four tasks and isolating network capacity as the key limiting factor on HalfCheetah. Furthermore, DWCs exhibit structurally sparse and interpretable connectivity patterns, enabling a direct inspection of which input thresholds influence control decisions.

1. Introduction

Deep Learning has transformed countless fields, from natural language processing (Vaswani et al., 2017; Radford et al., 2019) and computer vision (Krizhevsky et al., 2012; Dosovitskiy, 2021) to game playing (Mnih et al., 2013; Silver et al., 2016). The paradigm has successfully been transferred to continuous control as *deep reinforcement learning* (RL), where neural network policies serve as real-valued function approximators, trained to solve highly complex tasks, such as quadrotor racing (Kaufmann et al., 2023), robot locomotion (Miller et al., 2025), and even fusion-plasma control (Degraeve et al., 2022).

¹ISTA (Institute of Science and Technology Austria), 3400 Klosterneuburg, Austria. Correspondence to: Fabian Kresse <fabian.kresse@ist.ac.at>.

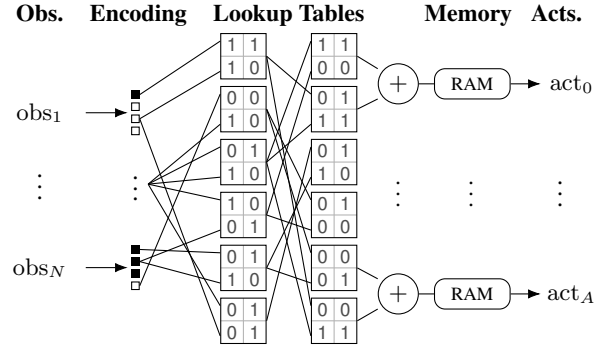


Figure 1. Differentiable Weightless Controllers (DWCs): real-valued observations are thermometer-encoded into bitvectors, processed by two layers of multi-input boolean-output lookup tables (here drawn with 2 inputs), aggregated by group summation, and mapped via per-action memory lookups to final action values.

However, policies implemented as neural networks rely on large numbers of compute-intensive multiply and accumulate operations, making their applications on resource-constrained hardware platforms, such as UAVs and mobile robots, difficult. In such cases, policies implemented as small and discrete-valued functions are preferable, as these allow efficient implementation on embedded hardware, such as FPGAs.

Because low-precision floating point or integer-only operations have efficiency advantages even on high-end GPUs, several prior works have studied either converting standard-trained deep networks into a *quantized* representation (post-training compressions, PTQ), or learning deep networks directly in quantized form (quantization-aware training, QAT), see e.g. Gholami et al. (2022) for a recent survey. However, most such works target a static supervised or next-word-prediction setting, in which the input and output domains are discrete to start with, and the task involves predicting individual outputs for individual inputs.

The setup of *continuous control*, i.e. learning control policies for cyber-physical systems such as autonomous robots or wearable devices, is more challenging, because input *states* and output *actions* can be continuous-valued instead of categorical, and the controller is meant to be run repeatedly over long durations, such that even small errors in the

control signal might accumulate over time.

Consequently, only few methods for quantized policy learning have been proposed so far. [Krishnan et al. \(2022\)](#) discuss PTQ from a perspective of reducing resources during training in RL and, in QAT ablations, find that low-bit quantization often does not harm returns. [Ivanov et al. \(2025\)](#) investigate both QAT and pruning (i.e., reducing the number of weights) jointly, finding that the combination of high sparsity and 8-bit weight quantization does not reduce control performance. Very recently, [Kresse & Lampert \(2025\)](#) showed that controllers can be trained using QAT with neurons that have weights and internal activation values of only 2 or 3 bits; we evaluate our approach against this baseline in the experiment section.

In this work, we challenge the necessity of relying on *weight-based* neural networks, i.e., those that rely on large matrix multiplications during inference, for learning continuous control policies. Instead, we introduce *DWCs* (*Differentiable Weightless Controllers*), a symbolic-differentiable architecture for continuous control in which dense matrix multiplication is replaced with sparse boolean logic. Figure 1 illustrates the inference pipeline.

At their core lie *differentiable weightless networks* (DWNs) ([Bacellar et al., 2024](#)), an FPGA-compatible and alternative variant of *logic-gate networks* (LGNs) ([Petersen et al., 2022](#)) that were originally proposed for high-throughput, low-energy classification tasks. We extend the DWN architecture to the continuous RL domain, enabling synthesis of control policies that are digital circuits instead of real-valued functions. Specifically, we introduce a data-adaptive input encoding that converts real-valued input signals into binary vectors, and a trainable output decoding that converts binary output vectors into real-valued actions of suitable range and scale. The resulting DWCs are compatible with gradient-based RL, and we demonstrate experimentally that the learned DWCs match weight-based neural network baselines (full precision or quantized) on standard MuJoCo benchmarks, including the high-dimensional Humanoid task.

At deployment time, DWCs process continuous observations by quantizing them using quantile binning and thermometer encoding, resulting in a fixed-width bitvector representation for each observation dimension. The bitvectors are concatenated and processed by a DWN, which consists of sparsely-connected layers of boolean-output lookup tables (LUTs) ([Bacellar et al., 2024](#)). The final layer produces a fixed number of bit outputs per action dimension. These are summed using a *popcount* operation and converted to a final action value using a single-cycle (SRAM) memory lookup.

As a consequence, DWCs are compatible with embedded

hardware platforms, especially FPGA platforms that explicitly support LUT operations. Here, DWCs can run with few- or even single-cycle latency and minuscule (e.g. Nanojoule-level) energy per operation, as we demonstrate for the case of an AMD Xilinx Artix-7.

Besides their efficiency, DWCs also have high potential for interpretability, because they consist of sparse, discrete, and symbolic elements instead of dense, continuous, matrix-multiplications in standard networks. For instance, the sparse connectivity in the first layer allows for direct identification of the input dimensions and thresholds utilized by the controller.

Contributions. To summarize, **our main contribution is the symbolic-differentiable DWC architecture** that extends previous DWNs from classification to continuous control tasks. We demonstrate that

- DWCs can be trained successfully using standard RL algorithms, reaching parity with floating-point policies (full precision or quantized) in most of our experiments.
- DWCs are orders of magnitude more efficient than previously proposed architectures, achieving few- or even single-clock-cycle latency and nanojoule-level energy cost per action when compile to FPGA hardware.
- DWCs allow for straightforward interpretation of some aspects of the policies they implement, specifically which input dimensions matter for the decisions, and what the relevant thresholds are.

2. Background

We briefly review deep reinforcement learning for continuous control, and provide background details on DWNs.

2.1. Reinforcement Learning (RL)

Reinforcement learning studies how an agent can learn, through trial and error, to maximize *return* (cumulative reward) while interacting with an environment ([Sutton & Barto, 2018](#)). There exist various reinforcement learning algorithms that are compatible with our setting of continuous control (continuous actions and observations). In the main body of this work we investigate the performance of DWCs with the state-of-the-art *Soft-Actor Critic* (SAC) method ([Haarnoja et al., 2018](#)). Results for *Deep Deterministic Policy Gradient* (DDPG) ([Lillicrap et al., 2016](#)) and *Proximal Policy Optimization* (PPO) ([Schulman et al., 2017](#)) can be found in Appendix B.

SAC is an off-policy method, which keeps a buffer of previous state transitions and taken actions. It updates the parameters of the policy network based on this buffer with advantage estimations from two auxiliary networks (called

critics). Actions during training are sampled stochastically from a normal distribution, parametrized as $\mathcal{N}(\mu_\theta, \sigma_\theta)$, with θ being learned parameters. During deployment, the mean action is used deterministically.

2.2. Differentiable Weightless Neural Networks

Weightless networks (Aleksander, 1983; Ludermir & de Oliveira, 1994) rely on table lookups instead of arithmetic (specifically matrix multiplications): each neuron is a lookup table (LUT) with k binary inputs and a single-bit output. Because each LUT input is connected to precisely one of the preceding layer outputs, this structure results in a sparsely connected computation graph. Signals remain binary throughout the network, enabling multiplication-free inference that maps directly to LUTs available on FPGAs. For the special case of $k = 2$ (two binary inputs per neuron), one recovers the case of logic-gate networks (Petersen et al., 2022).

Although traditional weightless networks were hard to train due to their discrete, non-differentiable structure, recently Bacellar et al. (2024) introduced a way to construct efficient surrogate gradients and a learnable interconnect, calling the resulting networks *Differentiable Weightless Networks* (DWNs). Below, we summarize the DWN forward and training mechanisms.

Thermometer encoding. DWNs operate on binary signals, so any real-valued observation has to be discretized. For any input $x \in \mathbb{R}$ and predefined thresholds $\tau_1 < \dots < \tau_B$, define the *thermometer* encoding (Carneiro et al., 2015),

$$E(x) = [1\{x \geq \tau_1\}, \dots, 1\{x \geq \tau_B\}] \in \{0, 1\}^B.$$

For d -dimensional signals, each dimension is encoded individually, and the results are concatenated, yielding a $B \times d$ -dimensional bitvector overall.

Logic Layers. A DWN with L layers comprises binary activation maps $b^{(\ell)} \in \{0, 1\}^{D_\ell}$, $\ell = 0, \dots, L$. Where D_0 is the size of the encoded input, and for $\ell > 0$, D_ℓ denotes the number of LUTs in layer ℓ . Each LUT is a boolean function with arity k . For LUT i we form an address $a_i^{(\ell+1)} \in \{0, 1\}^k$ by selecting k bits from $b^{(\ell)}$:

$$a_i^{(\ell+1)} = (b_{c_1}^{(\ell)}, \dots, b_{c_k}^{(\ell)}).$$

The selection indices (c_1, \dots, c_k) define the *interconnect*. They are learned via straight-through estimation during training, as described in Bacellar et al. (2024). While Bacellar et al. (2024) only train the first layers interconnect, we also make the later ones learnable. This is inspired by results in Kresse et al. (2025b), where training accuracy consistently improves if later-layer interconnects are learnable. Each LUT stores a table, T , of 2^k binary values. The output bit is the addressed entry,

$$b_j^{(\ell+1)} = T_i^{(\ell+1)}[\text{addr}(a_j^{(\ell+1)})],$$



Figure 2. DWC thermometer threshold positions.

where $\text{addr}(\cdot)$ maps the k -bit vector to its integer index. Concatenating all output bits yields $b^{(\ell+1)}$.

Group aggregation. To allow for multi-dimensional outputs, the final binary features $b^{(L)}$ of a DWN are partitioned into disjoint groups. For a group G , a *group sum* is computed,

$$s_G = \frac{1}{\tau} \sum_{i \in G} b_i^{(L)},$$

with a temperature $\tau > 0$ used as a scale during training. For classification, these s_G serve as logits for a softmax; at inference, the operation reduces to efficient popcount and argmax operations.

Gradient surrogate. Because the forward pass is discrete, DWNs rely on surrogate gradients for training. We follow Bacellar et al. (2024), who propose an *extended finite-difference* (EFD) estimator that perturbs the LUT address and aggregates contributions from all possible addresses with weights proportional to their Hamming distances.

3. Differentiable Weightless Controllers

We now provide details on how DWCs extend DWNs to continuous control tasks. In terms of architecture, we adapt the input quantization, such that it can deal with changing input distributions during training, and we adapt the output layer to allow for multi-dimensional continuous actions. Subsequently, we describe the RL training procedure.

3.1. Input Encoding

We map observations to binary inputs via clipped normalization and thermometer encoding. For each dimension j , we normalize with running mean and standard deviation, subsequently clipping: $\hat{x}_j = \text{clip}((x_j - \mu_j)/\sigma_j, -10, 10)$. While in deep RL, normalization is often considered optional, we employ it *always*, as we are projecting from \mathbb{R} to a restricted, a priori known interval, for which we can subsequently choose thermometer thresholds E_j . After normalization, we employ the same thermometer thresholds for all dimensions d_{in} .

Using an *odd* number of bits B , we place thresholds at stretched-Gaussian quantiles: let $q_m = m/B$ for $m = 1, \dots, B-1$ and an additional quantile at $\frac{1}{2}$, and set a stretch factor

$$s = \frac{10}{|\Phi^{-1}(\frac{1}{B})|},$$

where Φ^{-1} is the inverse cumulative probability distribution of the standard Gaussian. Define $\tau_{j,m} = s \Phi^{-1}(q_m)$ for

$m = 1, \dots, B$ so that the first/last thresholds land exactly at ± 10 , and the additional threshold at 0. The thermometer code is $E_j(\hat{x}_j) = [1\{\hat{x}_j \geq \tau_{j,1}\}, \dots, 1\{\hat{x}_j \geq \tau_{j,B}\}] \in \{0, 1\}^B$, concatenated over j to form $b^{(0)}$ for the first DWN layer. Figure 2 illustrates the resulting input thresholds.

3.2. Continuous-control head

To produce continuous actions we reinterpret the group aggregation as a bank of scalar heads, one per action dimension. Let $\{G_1, \dots, G_{d_{\text{act}}}\}$ be a partition of the final bits $b^{(L)}$. For dimension d we first normalise the group sum:

$$z_d = \frac{s_{G_d}}{|G_d|} - \frac{1}{2} \in \left[-\frac{1}{2}, \frac{1}{2}\right]. \quad (1)$$

We then apply a per-dimension affine transformation:

$$l_d = \alpha_d z_d + \beta_d,$$

with learnable scales $\alpha_d > 0$ and bias $\beta_d \in \mathbb{R}$. To ensure positive α_d , we parameterize $\alpha_d = e^{\alpha_{d,p}}$. This head is fully differentiable and integrates with policy-gradient objectives. The emitted l_d is the generated logit, which is passed through an additional tanh in the case of SAC before computing the final action. The initialization value of α_d restricts the initial policy actions to a subinterval of the possible action space. This is comparable to initializing the final layer parameters with a low standard deviation, a strategy that has been shown to improve learning in RL (Andrychowicz et al., 2020).

At deployment, the initial threshold operations required for the thermometer encoding should be implemented in a platform-dependent way. Commonly, actual sensor readings are obtained as integers from an *analog-to-digital converter* (ADC), in which the initial bitvector $b^{(0)}$ can be computed as fixed integer-to-thermometer lookup per sensor channel (the constants used for normalization and clipping are fixed after training, so they can be folded into the threshold values).

Subsequently, actions can be computed using only LUT evaluations, popcounts and SRAM memory lookups: starting with $b^{(0)}$, the bitvectors propagate through L LUT layers to produce $b^{(L)}$. For each action head d , we popcount its group G_d to obtain the integer s_{G_d} . An SRAM then implements the mapping from this popcount to the emitted control word, i.e., $s_{G_d} \mapsto \alpha_d(s_{G_d}/|G_d| - \frac{1}{2}) + \beta_d$ and, e.g. for SAC, the subsequent tanh. In practice, the table would output an integer actuator command. Note that, unlike the standard DWN classification head, no temperature parameter τ is required, simplifying hyperparameter tuning.

3.3. Training

The learnable components of DWCs are the LUT entries, their connectivity, and the mapping from popcounts to action

Table 1. Policy returns in different environments (median and the 25% and 75% quantiles over 10 trained models) for the proposed DWCs, standard floating point (FP), and low-precision quantized networks (Quant) of Kresse & Lampert (2025). Highest values are marked in bold. DWC returns are comparable to FP and at least as good as Quant across four of the five tasks (all except HalfCheetah).

| Environment | FP | Quant | DWC |
|-------------|--|--------------------------------|-------------------------------------|
| Ant | 5.6k _[4.3k, 5.8k] | 4.7k _[3.9k, 4.9k] | 5.7k _[5.5k, 5.9k] |
| HalfCheetah | 11.5k _[10.1k, 11.9k] | 10.5k _[9.6k, 11.0k] | 7.5k _[7.1k, 7.9k] |
| Hopper | 2.8k _[2.1k, 3.3k] | 1.9k _[1.1k, 3.3k] | 3.1k _[2.8k, 3.4k] |
| Humanoid | 6.2k _[6.0k, 6.7k] | 6.0k _[5.8k, 6.1k] | 6.1k _[5.8k, 6.6k] |
| Walker2d | 5.0k _[4.7k, 5.2k] | 4.7k _[4.4k, 5.0k] | 5.0k _[4.5k, 5.2k] |

values. The latter are parameterized as an affine transformation, potentially followed by an additional hyperbolic tangent, so standard gradient-based learning is applicable. To learn the former two in a differentiable way, we rely on the connection learning and the extended finite difference surrogate gradients of Bacellar et al. (2024), making DWCs overall compatible with any gradient-based reinforcement learning algorithm.

Note that, similar to previous work on quantized neural networks (Kresse & Lampert, 2025), during RL training we *only* parametrize the policy networks as DWCs, because only these are required at deployment time. All auxiliary networks, such as the critic networks and the σ_θ head for SAC can remain as standard floating-point networks.

4. Experiments

We evaluate the proposed Differentiable Weightless Controllers on five MuJoCo tasks (Todorov et al., 2012): Ant-v4, HalfCheetah-v4, Hopper-v4, Humanoid-v4 and Walker2d-v4, using SAC for training. We also investigate returns for DDPG and PPO in Appendix B.

Baselines. As baselines, we use two weight-based neural network setups: First, we use full-precision (FP) models trained with the CleanRL implementation (Huang et al., 2022) of SAC, as reported in Kresse & Lampert (2025). Here, the network has 256 neurons in the hidden layer. In contrast to the original CleanRL implementation, the networks use running input normalization, as this has been found to improve return for SAC for our tasks. Second, we compare against the QAT-trained low-precision models (2- or 3-bit weights and activations) from Kresse & Lampert (2025), which were designed to match the FP baselines at more compact network sizes.

DWC. We adopt the same architectures as in the baseline implementations, except that we use DWCs for the policy networks. Unless stated otherwise, DWCs are instantiated with two layers of $k=6$ input LUTs. We employ 1024 LUTs

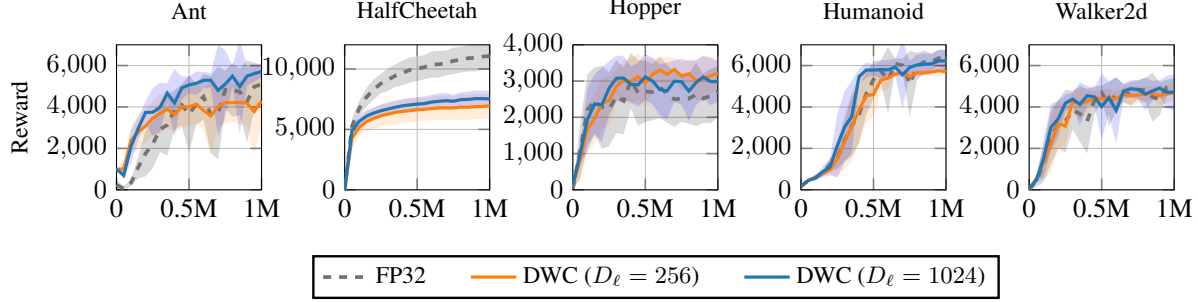


Figure 3. Mean return and standard deviation for ten models evaluated across the training steps, ten evaluation episodes per datapoint and model. Except for HalfCheetah (see main text), training trajectories are comparable to the FP baseline.

| | Environment | Reward | LUTs | FFs | B | DSP | Lat [μ s] | P [W] | TP | E.p.A. [J] |
|-------------------------|-------------|---------------------------------------|------|------|-----|-----|----------------|-------|-------------------|----------------------|
| $D_\ell = 256$ | Ant | 4.5k _[3.4k, 5.2k] | 0.8k | 0.5k | 0 | 0 | 0.01 | 0.105 | 1.0×10^8 | 1.1×10^{-9} |
| | HalfCheetah | 7.1k _[6.0k, 7.9k] | 0.8k | 0.4k | 0 | 0 | 0.01 | 0.105 | 1.0×10^8 | 1.1×10^{-9} |
| | Hopper | 3.3k _[3.0k, 3.5k] | 0.9k | 0.3k | 0 | 0 | 0.01 | 0.116 | 1.0×10^8 | 1.2×10^{-9} |
| | Humanoid | 5.7k _[5.5k, 5.8k] | 0.9k | 1.1k | 0 | 0 | 0.01 | 0.102 | 1.0×10^8 | 1.0×10^{-9} |
| | Walker2d | 4.6k _[4.5k, 4.7k] | 0.8k | 0.4k | 0 | 0 | 0.01 | 0.107 | 1.0×10^8 | 1.1×10^{-9} |
| $D_\ell = 1024$ | Ant | 5.7k _[5.5k, 5.9k] | 3.2k | 1.7k | 0 | 0 | 0.02 | 0.225 | 1.0×10^8 | 2.3×10^{-9} |
| | HalfCheetah | 7.5k _[7.1k, 7.9k] | 3.0k | 2.2k | 0 | 0 | 0.03 | 0.208 | 1.0×10^8 | 2.1×10^{-9} |
| | Hopper | 3.1k _[2.8k, 3.4k] | 3.2k | 2.0k | 0 | 0 | 0.03 | 0.228 | 1.0×10^8 | 2.3×10^{-9} |
| | Humanoid | 6.1k _[5.8k, 6.6k] | 3.2k | 3.7k | 0 | 0 | 0.02 | 0.219 | 1.0×10^8 | 2.2×10^{-9} |
| | Walker2d | 5.0k _[4.5k, 5.2k] | 2.8k | 2.1k | 0 | 0 | 0.03 | 0.206 | 1.0×10^8 | 2.1×10^{-9} |
| Kresse & Lampert (2025) | Ant | 4.7k _[3.9k, 4.9k] | 2.7k | 4.5k | 3 | 45 | 2.29 | 0.39 | 4.4×10^5 | 8.9×10^{-7} |
| | HalfCheetah | 10.5k _[9.6k, 11.0k] | 4.3k | 4.6k | 15 | 11 | 243.23 | 0.33 | 4.1×10^3 | 8.0×10^{-5} |
| | Hopper | 1.9k _[1.1k, 3.3k] | 2.4k | 2.0k | 0 | 45 | 0.21 | 0.31 | 4.8×10^6 | 6.5×10^{-8} |
| | Humanoid | 6.0k _[5.8k, 6.1k] | 2.3k | 3.1k | 1.5 | 45 | 15.36 | 0.33 | 6.5×10^4 | 5.1×10^{-6} |
| | Walker2D | 4.7k _[4.4k, 5.0k] | 1.9k | 1.6k | 2 | 4 | 162.23 | 0.17 | 6.2×10^3 | 2.8×10^{-5} |

Table 2. Post-synthesis resource utilization for one synthesized model, BRAM (B), end-to-end latency (Lat) in microseconds, power estimated by the Xilinx Power Estimator (P) in Watts, peak throughput (TP) in actions per second, and energy per action (E.p.A.) in Joule on a Artix-7 XC7A15T-1 at 100 MHz. Shown reward is the median over all ten models.

per layer, padding the last layer with LUTs to be divisible by the action dimension. Observations are discretized to 63 thermometer thresholds per dimension, as described in Section 3. Ablation studies on these choices are available in Section 5.

Hyperparameters. We adopt the protocol used in CleanRL, hence we use the same hyperparameters across each algorithm for all investigated tasks. For training the DWCs we use the same hyperparameters as for the baselines, as specified in Appendix C.

Training and Evaluation. For each configuration, we train 10 models with different random seeds. Each model is trained for 1 million environment steps and then its undiscounted return is estimated from 1000 rollouts of the fixed policy from random starting states. Compared to the default CleanRL implementation, we perform all evaluation rollouts without exploration noise.

4.1. Results: Quality

Figure 3 shows the training dynamics of DWCs versus the FP baseline. Table 1 shows the resulting returns after training, also including results for quantized networks. Clearly, DWCs learn policies of comparable quality to the floating point networks, and hence they can readily serve as more drop-in replacements, from a reward perspective. An exception is the HalfCheetah environment, where we observe a substantial return gap. Note that models with a cumulative reward of 7.5k on HalfCheetah are not performing badly at all, indeed they learn to *run*, i.e. master the environment. However, they do so at a slower pace than, e.g., the FP models with 11.5k reward.

Our findings confirm the observation from Kresse & Lampert (2025) that HalfCheetah is the task most resistant to network reduction and quantization, presumably because the task is *capacity-limited*. We study this phenomenon further in Section 5 and the Appendix.

4.2. Noise Robustness

Following Duan et al. (2016), we also assess the robustness of DWCs to observation noise. We inject zero-mean Gaussian noise with standard deviations $\sigma \in \{0.1, 0.2, 0.3, 0.4, 0.5\}$ into normalized observations (unit variance) and compare DWCs to the FP baseline and the quantized noise robustness results from Kresse & Lampert (2025). Figure 5 reports the results, which show that DWCs achieve noise robustness profiles comparable to that of the quantized network, and generally on the same level as or even better than floating point networks. The only exceptions are the compact ($D_\ell = 256$) models, which perform worse on Humanoid under high noise.

4.3. Results: Efficiency

The main advantage of DWCs over standard deep controllers is that they consist exclusively of elements that have direct representations on low-energy hardware platforms. To demonstrate this, we perform synthesis and implementation (place-and-route) of the resulting networks for an FPGA, reporting required resources and energy estimates based on the manufacturer-provided tools.

We run out-of-context (OOC) synthesis and implementation with the AMD Vivado toolchain (2022.2), targeting an AMD Xilinx Artix-7 XC7A15T (speed grade -1), see Table 10 in Appendix F for the available device resources. Note that the selected FPGA only has a total of 10,400 LUT-6s and twice this amount of flip-flops (FFs), which is a much smaller FPGA than previous investigations of DWNs (Bacellar et al., 2024). Instead, our setup is directly comparable to Kresse & Lampert (2025), who used the same reference FPGA platform and tool chain.

We target a clock frequency of 100 MHz, inserting up to two pipeline stages—the first one between the two LUT layers, and the second one before the popcount—until we meet the desired timing. As our design is implemented OOC we do not consider any overhead due to I/O interfaces. Furthermore, we assume that all observation normalization steps and the final BRAM lookup for the action scaling take place outside of the FPGA, because these depend on the specific application (e.g. the input format depends on the type of ADCs, the output format on the type of DACs).

Table 2 reports Reward, LUTs, FFs, BRAMs (B), Latency (Lat), Power (P), Throughput (TP), and Energy per Action (E.p.A) for each setup. Since full precision policies are not practical on the selected hardware, we compare to the quantized networks from Kresse & Lampert (2025). The only difference to their setup is that our values for power estimation are based on the toolchain’s post-implementation power report, rather than the less accurate Vivado Power Estimator.

The results show that DWCs exhibit orders of magnitude lower latency and energy per action compared to the low-bitwidth quantized networks. For our standard $D_\ell = 1024$ setup, latency is only 2 or 3 clock cycles, the throughput is the maximal possible of 10^8 actions per second, and the energy usage is in the range of 2 Nanojoule per action. In contrast, Kresse & Lampert (2025) reports orders of magnitude higher and much more heterogeneous resource usage: their latencies range from 21 cycles to over 162,000 cycles, their throughput between 4.1×10^3 and 4.8×10^6 actions per second, and their energy usage per action between 2.8×10^{-5} and 6.5×10^{-8} Joule.

Additionally, in contrast to the quantized models, the computational core of DWCs does not require any BRAM or DSP resources, making them deployable on even more limited hardware than the already small FPGA investigated here.

To illustrate the scaling behavior, we include results for even smaller DWCs with layer width $D_\ell = 256$ in Table 2. This results in single-clock-cycle latency, still maximum throughput, and energy usage per action reduced further by a factor of approximately 2.

5. Ablation Studies and Model Interpretability

In this section we report ablation studies on the scaling behavior of DWCs with respect to their layer widths and the input size to the LUTs. Subsequently, we demonstrate how the sparse binary nature of DWCs allows for insights into their learned policies.

5.1. Network Capacity

We first investigate the effect of different network capacities. Concretely, we study the effect of varying the layer sizes (widths) and the number of inputs to each LUT. Further ablations on the impact of input resolution and number of layers are available in Appendix E.

Layer Width. Assuming that the number of layers is fixed, a large impact on the network capacity comes from the layer width, D_ℓ , i.e. the number of LUTs. We run experiments in the previous setting with layer width varying across $\{128, 256, 512, 1024, 2048, 4096\}$, where the last layer is padded to be divisible by the action dimension, and report the results in Figure 4. For four of the tasks, the quality is relatively stable with respect to layer widths, with per-layer sizes above 256 generally exhibiting returns similar to the floating-point baseline. This indicates that these learning tasks are not capacity limited, but that at the same time no overfitting effects seem to emerge. As previously observed, HalfCheetah is an exception, where we observe that the quality of the policy increases monotonically with the width of the layers. There are two possible explanations for this phenomenon observed on HalfCheetah: 1) smoother actions,

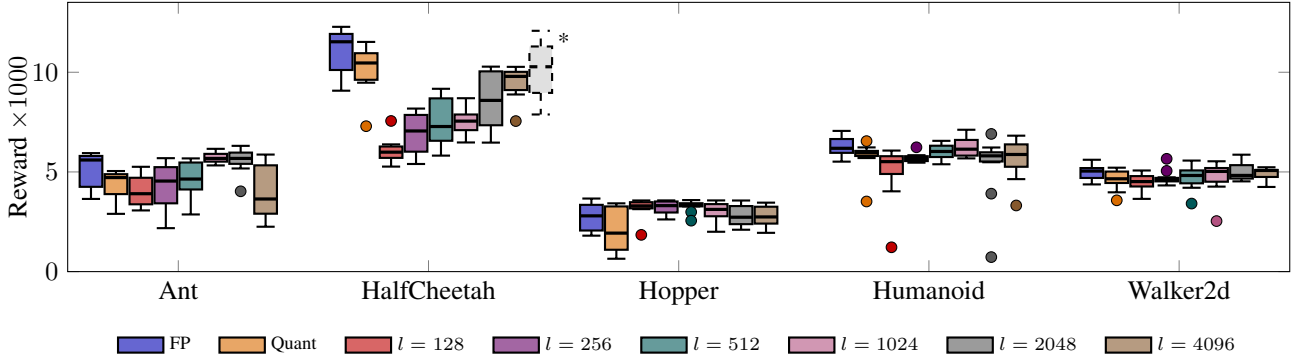


Figure 4. Policy returns for FP, Quant and DWCs with varying LUT layer widths. Generally, already models with 256 to 512 LUTs per layer achieve returns on par with the FP baseline. Only for HalfCheetah, we observe a monotonically increasing median return with increasing LUT layer width. * indicates a special high-capacity model with 16k-LUTs per layer and 255-bit per input dimension, see Section 5.

due to a higher output layer width, resulting in more possible actions, as each action head has a resolution of the size of the partition G_d ; and 2) higher representation capacity and input layer resolution, as more LUTs can connect to different bits in the first layer. In light of the results in Kresse & Lampert (2025) that a 3-bit resolution suffices for HalfCheetah in the output actions; and hidden capacity appears to be the major bottleneck in quantized neural networks, we hypothesize that 2) is the case.

To explore this further, we investigate a significantly larger DWC with $D_\ell = 16$, 384 LUTs per layer and inputs quantized to 255 levels (instead of 63). Due to the larger layer size, we do not train the second layer interconnect, but initialize it randomly and keep it fixed; the remaining training setup remains unchanged. Results are depicted in Figure 4 (dashed light gray entry). With a median return value above $10.3k$, this setup now matches the returns of the quantized baseline (median return $10.4k$) and falls within the region of uncertainty of the floating-point policy (median return $11.5k$). Notably, even at the increased layer width, DWCs requires only 32k lookups (and six popcounts, in the case of HalfCheetah)—substantially fewer than 70k+ multiply-accumulate operations by the two baselines. We take this result as evidence that DWNs can scale to such tasks, if required.

LUT Size Besides the number of LUTs, also the number of inputs per LUT, k , impacts the network capacity, as more inputs imply that layers are more densely connected, and that the LUTs themselves can express more complex relations. In Figure 8 in the appendix, we report average returns for all tasks with k varied from $\{2, 3, 4, 5, 6\}$ and constant layer width $D_\ell = 1024$. In line with the previous experiments, we observe capacity effects limiting returns only for HalfCheetah, while the other returns remain largely unaffected. This suggests that in practice, the number of LUT inputs can be chosen based on what matches the available hardware. For FPGAs, built-in support for $k = 6$ is common, whereas on

custom ASICs, any k larger than 2 could be prohibitively expensive.

5.2. Diagnostics and Interpretability

Deep networks are often criticized as *black boxes* (Molnar, 2020; Vouros, 2022), where the trained policy offers little insight into which feature values drive specific actions.

Here, we demonstrate how binary sparse DWCs can potentially contribute to overcoming this issue to some extent. Because input bits correspond to specific input thresholds and connections to processing LUTs are both sparse and learned, we can infer feature importance simply by counting outgoing connections. Figure 6 illustrates the number of connections received per observation dimension, averaged over the ten trained models ($D_\ell = 1024$). The entries are sorted after aggregation according to the mean number of connections. The data shows that connectivity is non-uniform: some input dimensions receive substantially more connections than others, especially for higher-dimensional observation tasks, i.e. Ant and Humanoid. The low standard deviations across independent models indicate that the network consistently identifies the same specific dimensions as relevant for solving the task.

Interestingly, for Humanoid, a large number of observation dimensions receive no connections at all (on average 275 out of 376 receive a connection). Because the trained model nevertheless attains performance comparable to the FP model, we conclude that the unconnected dimensions are not necessary for good control. In contrast, *torso velocity observations* receive the highest number of connections for Humanoid. As the reward function is heavily dependent on forward velocity, this suggests the DWC has identified the features most directly correlated with the reward signal.

Figure 7 shows the distribution of connections across input threshold bits, averaged over dimensions and over trained models. Recall that the input bit with index 31 out of 63

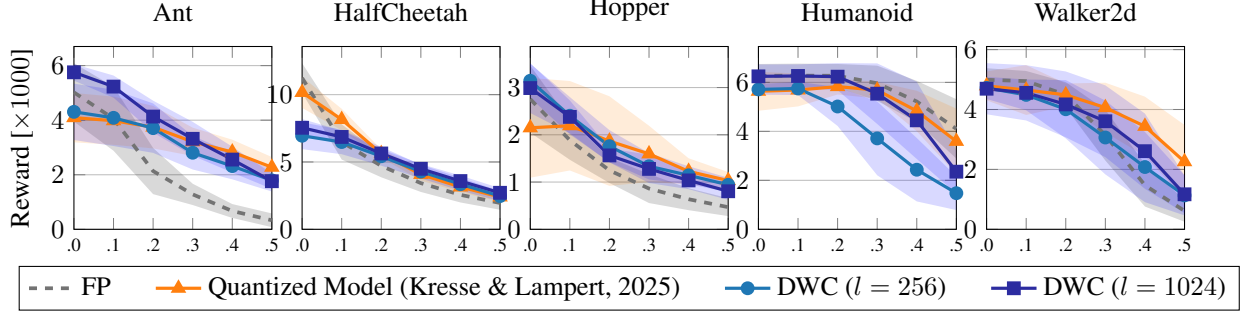


Figure 5. Reward performance under injected observation noise with varying noise level σ . Floating-point (FP), QAT policies from Kresse & Lampert (2025) and our DWCs on MuJoCo tasks. Bands show one standard deviation across trained models. The quantized models and DWCs perform better, or on par, with the FP baseline under injection, except for Humanoid, where the smaller DWCs show reduced rewards for larger noise.

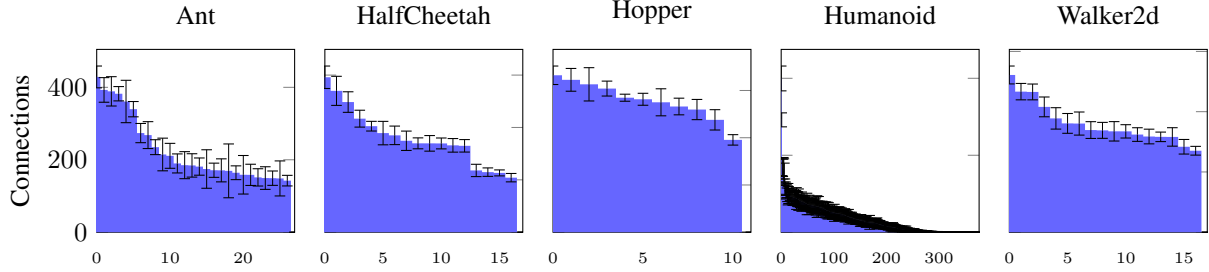


Figure 6. Number of connections received for (sorted) input dimension averaged over trained DWCs ($D_\ell = 1024$) for all five environments.

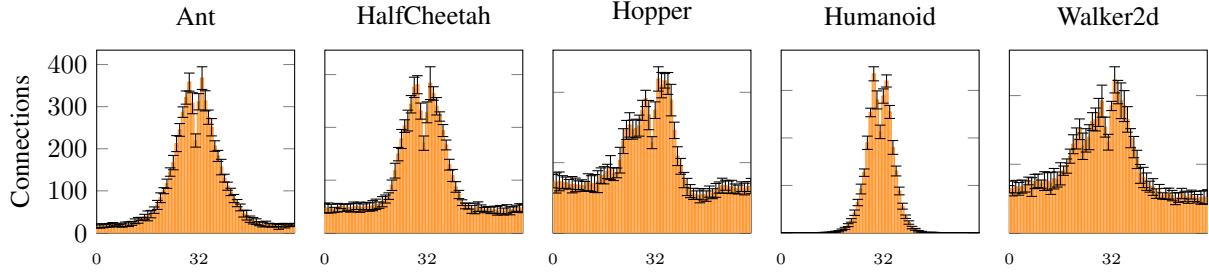


Figure 7. Distribution of connections per threshold bit index across all environments. We consistently observe a two-modal distribution slightly left and right of the center (index 31, corresponding to normalized observation value 0).

corresponds to the normalized observation value of 0, index 0 corresponds to the normalized value of -10 and index 63 to 10 (Section 3).

Perhaps unsurprisingly, the highest connectivity density is typically found around the normalized observation value of zero. However, instead of a Normal distribution, we observe two distinct modes left and right of the center. This is potentially explained by the reduced probability density captured by the 0 threshold, which is artificially inserted between the two thresholds to its left and right. Furthermore, some tasks (Hopper, Walker, and HalfCheetah) show heavier tails than the others (Ant, Humanoid). We hypothesize that the heavier tails are explainable by the lower observation dimensionality of their respective tasks, and not due to an increased importance of extreme observation values. This hypothesis is supported by Figure 11 in Appendix E, showing the same plot for DWCs with $D_\ell = 128$, which

generally exhibit similar return performance (see Figure 4). Here, the tails are lighter, with the maximal number of possible first-layer connections having been significantly reduced to just $k \times D_\ell = 768$, indicating that the heavier tails observed for the larger models are indeed due to the higher number of possible connections, suggesting that many connections might not be contributing significantly.

6. Summary and Discussion

In this work, we introduced DWCs (Differentiable Weightless Controllers), which are differentiable weightless networks adapted to handle continuous input states and output continuous actions. Furthermore, they can be trained using standard gradient-based reinforcement learning algorithms. DWCs allow for highly efficient implementation on low-energy embedded hardware, as we demonstrated by compiling them for an Xilinx Artix-7 FPGA at 100 MHz, where

the resulting networks have extremely low resource requirements at substantially lower inference time (2–3 clock cycle latency, even down to a single cycle for smaller DWCs; nanojoule-level energy usage per action). At the same time, they can achieve return parity with standard floating-point networks even on high-dimensional, difficult RL tasks.

Furthermore, we highlight the interpretability and capacity properties of DWCs through a sequence of experiments and ablation studies, particularly on the HalfCheetah environment, which is the most capacity-limited one of the studied MuJoCo tasks.

An existing limitation is the high computational cost at training time, which significantly exceeds the cost at deployment, because of the relaxations required to allow for gradient-based training. This aspect also means that training is currently only doable in simulated environments, not interactively on-device.

References

- Acharya, K., Raza, W., Dourado, C., Velasquez, A., and Song, H. H. Neurosymbolic reinforcement learning and planning: A survey. *IEEE Transactions on Artificial Intelligence*, 2023.
- Akiba, T., Sano, S., Yanase, T., Ohta, T., and Koyama, M. Optuna: A next-generation hyperparameter optimization framework. In *ACM SIGKDD International Conference on Knowledge Discovery & Data Mining*, 2019.
- Aleksander, I. Emergent intelligent properties of progressively structured pattern recognition nets. *Pattern Recognition Letters*, 1983.
- Anderson, G., Verma, A., Dillig, I., and Chaudhuri, S. Neurosymbolic reinforcement learning with formally verified exploration. *Conference on Neural Information Processing Systems (NeurIPS)*, 2020.
- Andrychowicz, M., Raichuk, A., Stańczyk, P., Orsini, M., Girgin, S., Marinier, R., Hussenot, L., Geist, M., Pietquin, O., Michalski, M., et al. What matters in on-policy reinforcement learning? a large-scale empirical study. *arXiv preprint arXiv:2006.05990*, 2020.
- Bacellar, A. T., Susskind, Z., Breternitz Jr, M., John, E., John, L. K., Lima, P. M., and França, F. M. Differentiable weightless neural networks. In *International Conference on Machine Learning (ICML)*, 2024.
- Bastani, O., Pu, Y., and Solar-Lezama, A. Verifiable reinforcement learning via policy extraction. *Conference on Neural Information Processing Systems (NeurIPS)*, 2018.
- Bühner, S., Plesner, A., Aczel, T., and Wattenhofer, R. Recurrent deep differentiable logic gate networks. *arXiv preprint arXiv:2508.06097*, 2025.
- Carneiro, H. C., França, F. M., and Lima, P. M. Multilingual part-of-speech tagging with weightless neural networks. *Neural Networks*, 2015.
- Chevtchenko, S. F. and Ludermitz, T. B. Combining STDP and binary networks for reinforcement learning from images and sparse rewards. *Neural Networks*, 2021.
- Degrave, J., Felici, F., Buchli, J., Neunert, M., Tracey, B., Carpanese, F., Ewalds, T., Hafner, R., Abdolmaleki, A., de las Casas, D., Donner, C., Fritz, L., Galperti, C., Huber, A., Keeling, J., Tsimpoukelli, M., Kay, J., Merle, A., Moret, J.-M., Noury, S., Pesamosca, F., Pfau, D., Sauter, O., Sommariva, C., Coda, S., Duval, B., Fasoli, A., Kohli, P., Kavukcuoglu, K., Hassabis, D., and Riedmiller, M. Magnetic control of tokamak plasmas through deep reinforcement learning. *Nature*, 2022.
- Dosovitskiy, A. An image is worth 16x16 words: Transformers for image recognition at scale. In *International Conference on Learning Representations (ICLR)*, 2021.
- Duan, Y., Chen, X., Houthoofd, R., Schulman, J., and Abbeel, P. Benchmarking deep reinforcement learning for continuous control. In *Proceedings of The 33rd International Conference on Machine Learning*, 2016.
- Gerlach, L., Kauffman, E., Våge, L. H., and Ojalvo, I. Rapid inference of logic gate neural networks for anomaly detection in high energy physics. *arXiv preprint arXiv:2511.01908*, 2025a.
- Gerlach, L., Våge, L., Gerlach, T., and Kauffman, E. WARP-LUTs-walsh-assisted relaxation for probabilistic look up tables. *arXiv preprint arXiv:2510.15655*, 2025b.
- Gholami, A., Kim, S., Dong, Z., Yao, Z., Mahoney, M. W., and Keutzer, K. A survey of quantization methods for efficient neural network inference. In *Low-power computer vision (LPCV)*. 2022.
- Graesser, L., Evci, U., Elsen, E., and Castro, P. S. The state of sparse training in deep reinforcement learning. In *International Conference on Machine Learning (ICML)*, 2022.
- Haarnoja, T., Zhou, A., Abbeel, P., and Levine, S. Soft actor-critic: Off-policy maximum entropy deep reinforcement learning with a stochastic actor. In *International Conference on Machine Learning (ICML)*, 2018.
- Huang, S., Dossa, R. F. J., Ye, C., Braga, J., Chakraborty, D., Mehta, K., and Araújo, J. G. CleanRL: High-quality

- single-file implementations of deep reinforcement learning algorithms. *Journal of Machine Learning Research (JMLR)*, 2022.
- Ivanov, D. A., Larionov, D. A., Maslennikov, O. V., and Voevodin, V. V. Neural network compression for reinforcement learning tasks. *Scientific Reports*, 2025.
- Kadokawa, Y., Tsurumine, Y., and Matsubara, T. Binarized p-network: Deep reinforcement learning of robot control from raw images on FPGA. *IEEE Robotics and Automation Letters*, 2021.
- Kaptein, M. *Interpretable Reinforcement Learning for Continuous Action Environments*. PhD thesis, Delft University of Technology, 2025.
- Kaufmann, E., Bauersfeld, L., Loquercio, A., Müller, M., Koltun, V., and Scaramuzza, D. Champion-level drone racing using deep reinforcement learning. *Nature*, 2023.
- Kim, Y. Deep stochastic logic gate networks. *IEEE Access*, 2023.
- Kresse, F. and Lampert, C. H. Learning quantized continuous controllers for integer hardware. *arXiv preprint arXiv:2511.07046*, 2025.
- Kresse, F., Yu, E., Lampert, C., and Henzinger, T. A. Logic gate neural networks are good for verification. In *International Conference on Neuro-symbolic Systems (NeuS)*, 2025a.
- Kresse, F., Yu, E., and Lampert, C. H. Scalable interconnect learning in boolean networks. *arXiv preprint arXiv:2507.02585*, 2025b.
- Krishnan, S., Lam, M., Chitlangia, S., Wan, Z., Barth-Maron, G., Faust, A., and Reddi, V. J. QuaRL: Quantization for fast and environmentally sustainable reinforcement learning. *Transactions on Machine Learning Research (TMLR)*, 2022.
- Krizhevsky, A., Sutskever, I., and Hinton, G. E. Imagenet classification with deep convolutional neural networks. In *Conference on Neural Information Processing Systems (NeurIPS)*, 2012.
- Lazarus, C. and Kochenderfer, M. J. Deep binary reinforcement learning for scalable verification. *arXiv preprint arXiv:2203.05704*, 2022.
- Lillicrap, T. P., Hunt, J. J., Pritzel, A., Heess, N., Erez, T., Tassa, Y., Silver, D., and Wierstra, D. Continuous control with deep reinforcement learning. In *International Conference on Learning Representations (ICLR)*, 2016.
- Lu, H., Alemi, M., and Rawassizadeh, R. The impact of quantization and pruning on deep reinforcement learning models. *arXiv preprint arXiv:2407.04803*, 2024.
- Ludermir, T. B. and de Oliveira, W. R. Weightless neural models. *Computer Standards & Interfaces*, 1994.
- Miller, A., Yu, F., Brauckmann, M., and Farshidian, F. High-performance reinforcement learning on spot: Optimizing simulation parameters with distributional measures. *arXiv preprint arXiv:2504.17857*, 2025.
- Miotti, P., Niklasson, E., Randazzo, E., and Mordvintsev, A. Differentiable logic cellular automata: From game of life to pattern generation. *arXiv preprint arXiv:2506.04912*, 2025.
- Mnih, V., Kavukcuoglu, K., Silver, D., Graves, A., Antonoglou, I., Wierstra, D., and Riedmiller, M. Playing atari with deep reinforcement learning. In *NeurIPS Deep Learning Workshop*, 2013.
- Molnar, C. *Interpretable machine learning*. lulu.com, 2020.
- Petersen, F., Borgelt, C., Kuehne, H., and Deussen, O. Deep differentiable logic gate networks. In *Conference on Neural Information Processing Systems (NeurIPS)*, 2022.
- Petersen, F., Kuehne, H., Borgelt, C., Welzel, J., and Ermon, S. Convolutional differentiable logic gate networks. In *Conference on Neural Information Processing Systems (NeurIPS)*, 2024.
- Radford, A., Wu, J., Child, R., Luan, D., Amodei, D., Sutskever, I., et al. Language models are unsupervised multitask learners. 2019.
- Schulman, J., Wolski, F., Dhariwal, P., Radford, A., and Klimov, O. Proximal policy optimization algorithms. *arXiv preprint arXiv:1707.06347*, 2017.
- Silva, A., Killian, T., Jimenez, I., Son, S.-H., and Gombolay, M. Optimization methods for interpretable differentiable decision trees applied to reinforcement learning. In *International conference on artificial intelligence and statistics (AISTATS)*, 2020.
- Silver, D., Huang, A., Maddison, C. J., Guez, A., Sifre, L., van den Driessche, G., Schrittwieser, J., Antonoglou, I., Panneershelvam, V., Lanctot, M., Dieleman, S., Grewe, D., Nham, J., Kalchbrenner, N., Sutskever, I., Lillicrap, T. P., Leach, M., Kavukcuoglu, K., Graepel, T., and Hassabis, D. Mastering the game of go with deep neural networks and tree search. *Nature*, 2016.
- Sutton, R. S. and Barto, A. G. *Reinforcement Learning: An Introduction*. MIT Press, 2018.

- Tan, Y., Hu, P., Pan, L., Huang, J., and Huang, L. RLx2: Training a sparse deep reinforcement learning model from scratch. In *IEEE International Conference on Robotics and Automation (ICRA)*, 2023.
- Todorov, E., Erez, T., and Tassa, Y. MuJoCo: A physics engine for model-based control. In *IEEE/RSJ international conference on intelligent robots and systems (IROS)*, 2012.
- Valencia, R., Sham, C.-W., and Sinnen, O. Using neuroevolved binary neural networks to solve reinforcement learning environments. In *IEEE Asia Pacific Conference on Circuits and Systems (APCCAS)*, 2019.
- Vaswani, A., Shazeer, N., Parmar, N., Uszkoreit, J., Jones, L., Gomez, A. N., Kaiser, L., and Polosukhin, I. Attention is all you need. In *Conference on Neural Information Processing Systems (NeurIPS)*, 2017.
- Vouros, G. A. Explainable deep reinforcement learning: state of the art and challenges. *ACM Computing Surveys*, 2022.
- Yousefi, S., Plesner, A., Aczel, T., and Wattenhofer, R. Mind the gap: Removing the discretization gap in differentiable logic gate networks. *arXiv preprint arXiv:2506.07500*, 2025.
- Yue, C. and Jha, N. K. Learning interpretable differentiable logic networks. *IEEE Transactions on Circuits and Systems for Artificial Intelligence*, 2024.

A. Related Work

Here, we discuss more related work regarding quantization and pruning for RL, and variants of weightless neural networks.

Pruning and Quantization for RL Previous work explored quantizing (Krishnan et al., 2022) and pruning deep continuous control RL policies, or both simultaneously (Ivanov et al., 2025; Lu et al., 2024)—which reduces their memory footprint and computational cost—showing that substantial pruning ($\geq 95\%$) (Graesser et al., 2022; Tan et al., 2023) and quantization of most of the network to 3 or 2-bits is possible without harming policy returns (Kresse & Lampert, 2025). Additionally, there has been work on binary, one-bit, quantized RL policies (Lazarus & Kochenderfer, 2022; Kadokawa et al., 2021; Chevtchenko & Ludermir, 2021; Valencia et al., 2019). However, these focus on discrete action spaces or only partially binarize the network. In contrast, our DWCs are fully one-bit policies for continuous control tasks, which has not been shown to be feasible in prior work.

Deep Boolean Networks (DBNs) Petersen et al. (2022) proposed *Differentiable Logic Networks* (Petersen et al., 2022), later extending them to a convolution-style architecture (Petersen et al., 2024), training layers of 2-input LUTs (boolean gates) end-to-end with gradient descent.

Since then there have been several extensions and variants of DLNs, improving various aspects. Notably, interconnect learning was introduced (Bacellar et al., 2024; Yue & Jha, 2024) and the original formulation, which required 2^{k^k} parameters for k -input LUTs was improved to only require 2^k parameters per LUT (Bacellar et al., 2024; Gerlach et al., 2025b). Various other improvements to scalability and convergence have also been performed (Kim, 2023; Yousefi et al., 2025; Yue & Jha, 2024).

Most commonly, DBNs have been applied to small-scale image and tabular classification tasks. Lately, this has been expanded to include anomaly detection (Gerlach et al., 2025a), recurrent image generation (Miotti et al., 2025), and recurrent language modeling (Bühner et al., 2025). In these applications, scalability to larger datasets has proven to be challenging, due to the high compute requirements during training, as in current work at least four floating point parameters are required per limited expressivity, boolean 2-input gate. Last DBNs have shown to be promising for formal verification (Kresse et al., 2025a). Networks for continuous control tasks, however, are typically small, and as they are safety-critical, could benefit greatly from formal verification, making them an ideal fit for DBNs as explored in this work.

Neuro-Symbolic Approaches for RL As our work touches upon the intersection of symbolic and neural methods, we very briefly review closely related work in this area. A more comprehensive overview can be found in (Acharya et al., 2023). Bastani et al. (2018) investigates continuous control, distilling policies into decision trees, their approach scales at least to HalfCheetah. Anderson et al. (2020) project policies to a symbolic space. In both approaches, the policy is not directly learned with gradient descent as we do here. Silva et al. (2020) and Kaptein (2025) directly learn a decision tree; however, it is not clear if this approach scales to high-dimensional continuous tasks. In contrast to these works, DWCs directly learn a propositional structure with gradient descent, which scales to high-dimensional continuous control tasks such as Humanoid.

B. DDPG and PPO returns

In this appendix we provide results for training DWCs with DDPG and PPO. Table 3 shows results for all investigated tasks and algorithms. For SAC and DDPG we use the same hyperparameters for both DWCs and the FP32 baseline. DWCs trained with DDPG use 1024 LUTs per layer. For PPO we perform hyperparameter tuning for both FP32 and DWCs separately, resulting in 256 LUTs per layer for DWCs. Hyperparameters and search details are provided in Appendix C.

For PPO we directly use the generated logit l_a as the action. While for DDPG, we compute the action with a tanh as in SAC.

For the DDPG FP baseline, we report results with *unnormalized* observations, as this outperforms observation normalization on our tasks (Kresse & Lampert, 2025). All other experiments (SAC, PPO) use observation normalization also for the FP model. While SAC shows very consistent results for FP and DWCs across all tasks, DDPG and PPO results vary, with DWCs sometimes outperforming and sometimes underperforming FP32. Overall, for DDPG the performance gap for HalfCheetah remains the largest, similar to SAC.

| Alg. | Environment | FP \pm sd | DWC \pm sd | FP median [q ₂₅ , q ₇₅] | DWC median [q ₂₅ , q ₇₅] |
|------|----------------|------------------|-----------------|--|---|
| SAC | Ant-v4 | 5.1k \pm 0.9k | 5.7k \pm 0.3k | 5.6k _[4.3k, 5.8k] | 5.7k _[5.5k, 5.9k] |
| | HalfCheetah-v4 | 11.1k \pm 1.2k | 7.5k \pm 0.7k | 11.5k _[10.1k, 11.9k] | 7.5k _[7.1k, 7.9k] |
| | Hopper-v4 | 2.7k \pm 0.7k | 3.0k \pm 0.6k | 2.8k _[2.1k, 3.3k] | 3.1k _[2.8k, 3.4k] |
| | Humanoid-v4 | 6.3k \pm 0.5k | 6.2k \pm 0.5k | 6.2k _[6.0k, 6.7k] | 6.1k _[5.8k, 6.6k] |
| | Walker2d-v4 | 5.0k \pm 0.4k | 4.7k \pm 0.9k | 5.0k _[4.7k, 5.2k] | 5.0k _[4.5k, 5.2k] |
| DDPG | Ant-v4 | 1.1k \pm 0.6k | 1.3k \pm 0.9k | 1.0k _[0.6k, 1.4k] | 1.4k _[1.0k, 1.6k] |
| | HalfCheetah-v4 | 11.2k \pm 0.6k | 7.4k \pm 0.8k | 11.3k _[10.9k, 11.4k] | 7.3k _[6.7k, 7.9k] |
| | Hopper-v4 | 2.3k \pm 0.8k | 2.0k \pm 0.4k | 2.2k _[2.0k, 3.0k] | 2.0k _[1.8k, 2.2k] |
| | Humanoid-v4 | 1.9k \pm 0.6k | 1.3k \pm 0.2k | 1.7k _[1.5k, 2.4k] | 1.2k _[1.1k, 1.2k] |
| | Walker2d-v4 | 1.7k \pm 0.5k | 2.1k \pm 0.8k | 1.5k _[1.4k, 1.8k] | 2.3k _[1.4k, 2.6k] |
| PPO | Ant-v4 | 0.9k \pm 0.4k | 1.6k \pm 0.1k | 0.7k _[0.6k, 0.9k] | 1.6k _[1.5k, 1.7k] |
| | HalfCheetah-v4 | 1.6k \pm 0.6k | 2.1k \pm 0.6k | 1.5k _[1.4k, 1.6k] | 2.1k _[1.6k, 2.5k] |
| | Hopper-v4 | 1.9k \pm 0.6k | 1.7k \pm 0.6k | 2.1k _[1.5k, 2.4k] | 1.9k _[1.5k, 2.0k] |
| | Humanoid-v4 | 0.5k \pm 0.0k | 0.5k \pm 0.0k | 0.5k _[0.5k, 0.6k] | 0.5k _[0.5k, 0.5k] |
| | Walker2d-v4 | 2.2k \pm 1.1k | 1.4k \pm 0.3k | 2.4k _[1.3k, 2.9k] | 1.3k _[1.1k, 1.6k] |

Table 3. Return performance for DWCs and FP baseline. Showing mean \pm standard deviation and median [25th percentile, 75th percentile] over 10 trained models. In contrast to SAC, results for DDPG and PPO are more inconsistent, with DWCs sometimes exceeding and sometimes falling short of FP performance.

C. Hyperparameters

Table 4 and Table 5 show SAC and DDPG hyperparameters, respectively. Table 6 shows the PPO floating-point hyperparameters used in our experiments, while Table 7 shows the PPO hyperparameters used for DWCs.

Major differences between FP and DWCs PPO hyperparameters are a $\times 10$ learning rate for DWCs, a lower entropy coefficient, and a lower max gradient norm. The initial log α is conceptually similar to the floating-point std parameter, which corresponds to the initialization of the policy network’s output variance.

Tables 8 shows the search space for the PPO hyperparameter tuning for DWCs, while Table 9 shows the search space for the PPO hyperparameter tuning for the FP baseline. Remaining hyperparameters were set to the values in Table 6, which correspond to CleanRL (Huang et al., 2022) defaults. Hyperparameter tuning was performed jointly across Ant, Hopper, Walker, and HalfCheetah, optimizing for return after 1M timesteps over 3 seeds. Hyperparameter search was performed with Optuna (Akiba et al., 2019) using the Tree-Structured Parzen Estimator with 100 trials. The hyperparameter search for DWCs took 25 days of compute, which we distributed over 10 GPUs.

Table 4. SAC hyperparameters.

| Hyperparameter | Value |
|--------------------------|--------------------|
| Total timesteps | 1,000,000 |
| Replay buffer size | 1×10^6 |
| Discount γ | 0.99 |
| Target smoothing τ | 0.005 |
| Batch size | 256 |
| Learning starts | 5×10^3 |
| Policy LR | 3×10^{-4} |
| Q-network LR | 1×10^{-3} |
| Policy update frequency | 2 |
| Target network frequency | 1 |
| Entropy | autotune |

D. LUT Input Ablation

Figure 8 shows an ablation over the LUT input size k from 2 to 6 inputs. Larger k increases the expressivity of each LUT, but also exponentially increases the number of parameters per layer.

Clearly, already $k = 2$ achieves good results across all tasks, being comparable for all except for HalfCheetah. For

Table 5. DDPG hyperparameters.

| Hyperparameter | Value |
|-------------------------|--------------------|
| Total timesteps | 1,000,000 |
| Learning rate | 3×10^{-4} |
| Replay buffer size | 1×10^6 |
| Discount γ | 0.99 |
| Target smoothing τ | 0.005 |
| Batch size | 256 |
| Exploration noise (std) | 0.1 |
| Learning starts | 2.5×10^4 |
| Policy update frequency | 2 |

Table 6. PPO FP hyperparameters.

| Hyperparameter | Value |
|----------------------------|-----------------------|
| Total timesteps | 1,000,000 |
| Learning rate | 7.82×10^{-4} |
| Number of environments | 1 |
| Steps per environment | 2048 |
| Number of minibatches | 32 |
| Update epochs | 10 |
| Discount γ | 0.99 |
| GAE λ | 0.95 |
| Clip coefficient | 0.2 |
| Entropy coefficient | 6.8×10^{-5} |
| Value function coefficient | 0.5 |
| Max gradient norm | 0.811 |
| Floating-point std | 0.00212 |
| Adam ϵ | 1×10^{-5} |
| Anneal LR | True |
| Norm advantages | True |
| Clip value loss | True |

Table 7. PPO DWCs hyperparameters. Not shown hyperparameter are equivalent to Table 6.

| Hyperparameter | Value |
|----------------------|-----------------------|
| Learning rate | 6.76×10^{-3} |
| Entropy coefficient | 3.37×10^{-4} |
| Max gradient norm | 1.92 |
| Initial log α | -3.18 |
| LUT width | 256 |

Table 8. Hyperparameter search space for DWCs.

| Hyperparameter | Search Space |
|----------------------|---|
| Learning rate | Log-uniform $[7 \times 10^{-4}, 10^{-2}]$ |
| Max gradient norm | Uniform $[0.5, 2.5]$ |
| Hidden layer size | Categorical $\{128, 256, 512\}$ |
| Entropy coefficient | Uniform $[0, 0.05]$ |
| Initial log α | Uniform $[-6.0, -0.3]$ |

HalfCheetah, we observed similar capacity-limited returns as we observed in our size ablation.

E. Input Layer Bit & Layer Number Ablation

Figure 9 shows an ablation over the number of thermometer bits used in the input layer. We observe that while performance suffers at 5 input threshold bits, policy performance does not completely collapse. For 63 bits and $l = 128$, Figure 11 shows

Table 9. Hyperparameter search space for FP baseline.

| Hyperparameter | Search Space |
|---------------------|---|
| Learning rate | Log-uniform $[7 \times 10^{-4}, 10^{-2}]$ |
| Max gradient norm | Uniform $[0.5, 2.5]$ |
| Entropy coefficient | Uniform $[0, 0.05]$ |
| Floating-point std | Uniform $[10^{-3}, 0.1]$ |

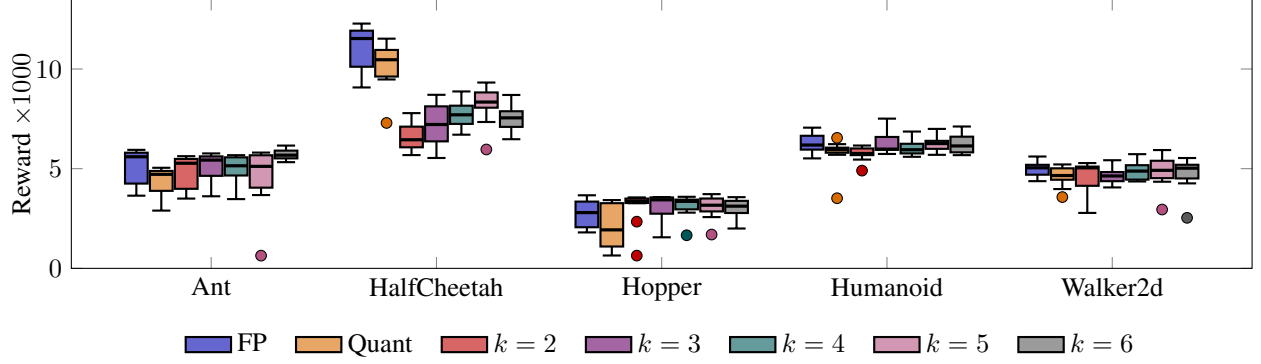


Figure 8. Showing floating-point (FP) baseline returns across environments and DWCs with varying LUT-inputs ($l = 1024$). Generally, already models with 2-input LUTs achieve returns comparable to the FP baseline. Only for HalfCheetah, we observe a generally monotonically increasing median return with increasing LUT table size.

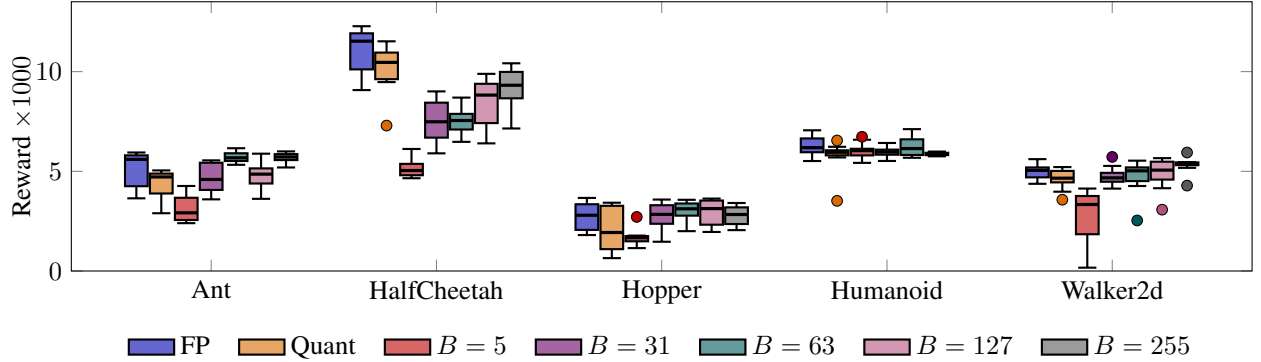


Figure 9. Showing floating-point baseline and DWCs return across environments with varying input bit width B . While having only 5 threshold bits per layer can harm policy performance. For most environments, 63 input bits suffice to saturate returns. As in other cases, the exception is HalfCheetah, which benefits monotonically from more fine-grained input binarizations.

the learned per-bit index connectivity for all environments. Figure 10 shows an ablation on the number of layers.

F. XC7A15T FPGA resources

Resources for the AMD Xilinx Artix-7 XC7A15T-FGG484-1 device are shown in Table 10.

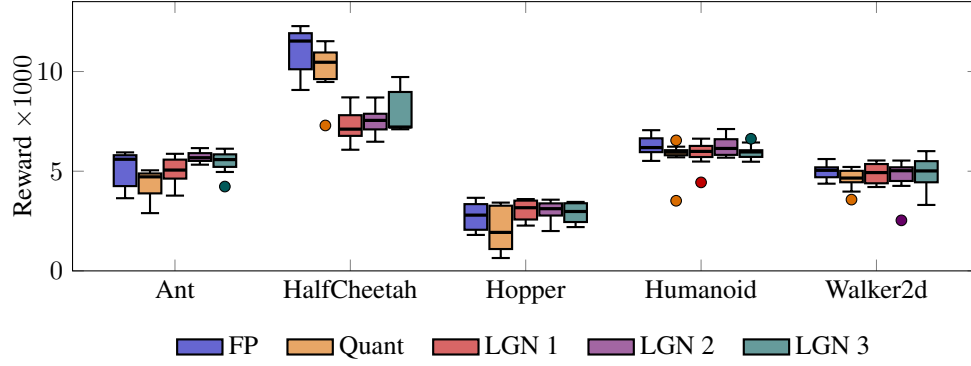


Figure 10. Showing floating-point baseline and DWCs return across environments with varying number of layers L . For $D_\ell=1024$, one layer generally suffices for attaining floating-point performance. Again, HalfCheetah, seems to benefit from additional layers, and hence, increased capacity.

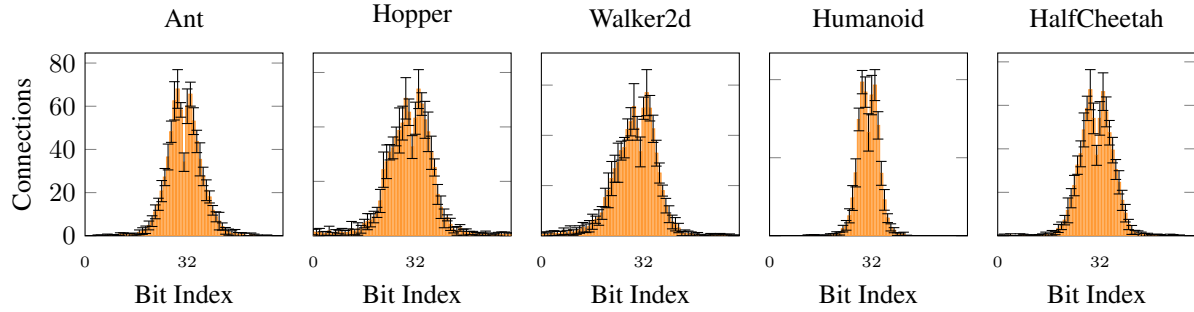


Figure 11. Distribution of connections per Bit Index across all environments. $l = 128$

Table 10. XC7A15T-FGG484-1 device resources.

| Resource | Quantity |
|-------------------|----------|
| LUTs | 10,400 |
| Flip-flops | 20,800 |
| DSPs | 45 |
| Block RAM (36 Kb) | 25 |
| Max user I/O pins | 250 |